Mechanics Research Communications 150 (2025) 104538

Contents lists available at ScienceDirect

Mechanics Research Communications

journal homepage: www.elsevier.com/locate/mechrescom

Nonlocal elastic plate problems via iterative method ☆

Andrea Caporale [a,b], Marzia Sara Vaccaro [c,*], Raffaele Barretta [c], Raimondo Luciano [d]

[a] Department of Civil and Mechanical Engineering, University of Cassino and Southern Lazio, via G. Di Biasio 43, Cassino, 03043, Italy
[b] European University of Technology, European Union
[c] Department of Structures for Engineering and Architecture, University of Naples Federico II, Via Claudio 21, Naples, 80125, Italy
[d] Department of Engineering, University of Naples Parthenope, via Amm. F. Acton 38, Naples, 80133, Italy

ARTICLE INFO

Keywords:
Nanoplates
Nonlocal continuum mechanics
Iterative methods

ABSTRACT

Elastostatics of nanoplates is addressed via an effective iterative procedure. An integral theory of elasticity is exploited to capture size effects in thin plates. The governing nonlocal elastic problem is represented by an integro-differential formulation, whose resolution is particularly demanding. Moreover, extending solution methodologies to general plate geometries and arbitrary boundary and loading conditions is a complex issue to address. To overcome these limitations, an effective iterative method is proposed. Such an algorithm relies solely on the solution of standard local elastostatic problems. Indeed, according to the iterative scheme, the nonlocal solution is obtained by solving a sequence of local problems. The presented methodology accommodates arbitrary nanoplate geometries and general kernels of the constitutive integral law, ensuring broad applicability and making it suitable for modeling a wide spectrum of nanoengineered systems.

1. Introduction

Miniaturized systems are attracting significant attention due to their outstanding features, including fast and highly sensitive responses, low power consumption and cost, and ease of integration into compact systems. Notably, nanoplates represent promising structural elements for small-scale devices (see e.g. [1–4]). Accurate modeling of small-scale structures requires advanced methodologies able to capture scale-dependent phenomena. In this context, nonlocal continuum mechanics provides a powerful tool for accounting for size effects into the mechanical response of nano-structures. In fact, it is well acknowledged that innovative materials and structures require advanced methodologies to capture non-conventional behaviors [5–15].

The first theories of nonlocal continuum mechanics were introduced in seminal works by Kröner [16], Krumhansl [17], Kunin [18] and Rogula [19,20]. An integral elasticity theory was then developed by Eringen [21,22], according to which the stress at a point is a spatial convolution driven by the elastic strain field, incorporating long-range interactions in nonlocal continua. However, the application of Eringen's theory to structural mechanic problems revealed paradoxical results, as first observed by Peddieson et al. [23].

To address these issues, Challamel and Wang [24] proposed a modified differential model based on a strain-driven two-phase law of elasticity. Nevertheless, when considering the limiting case of a fully nonlocal response, the resulting model was shown to be ill-posed. This pathological behavior was further analyzed by Benvenuti and Simone [25] and Khodabakhshi and Reddy [26], and finally resolved by Romano et al. [27], who demonstrated that the ill-posedness originates from an incompatibility between the equilibrium equations and the Eringen's integral constitutive law.

The above-mentioned issues were completely bypassed by Romano and Barretta [28] who introduced a stress-driven nonlocal integral model, in which the nonlocal elastic strain is formulated as a spatial convolution between the stress field and an averaging kernel. This alternative approach assures the well-posedness of the relevant structural problem while accurately accounting for long-range interactions and scale effects. The efficacy of the stress-driven model has been validated in several subsequent studies, such as the works contributed by Rezaiee-Pajand and Rajabzadeh-Safaei [29], Zhang et al. [30], Vaccaro et al. [31], Barretta et al. [32], Caporale et al. [33], Jafarinezhad et al. [34], Lovisi [35], Wang et al. [36], Lovisi et al. [37], Indronil [38], Alotta et al. [39], Behnam-Rasouli et al. [40] and Challamel and Sani [41]. A collection of achievements on mechanics of nonlocal elastic structures has been provided by Barretta et al. [42].

2. Motivation and outline

The elastostatic problem of nanoplates is governed by a set of integro-partial differential equations, which are generally difficult to

☆ This article is part of a Special issue entitled: 'Multiscale Metamaterials' published in Mechanics Research Communications.

* Corresponding author.
E-mail address: marziasara.vaccaro@unina.it (M.S. Vaccaro).

https://doi.org/10.1016/j.mechrescom.2025.104538
Received 31 July 2025; Received in revised form 20 September 2025; Accepted 9 October 2025
Available online 21 October 2025

solve. For a specific type of kernel and for axisymmetric nanoplates, the relevant problem can be conveniently converted into a set of differential equations equipped with constitutive boundary conditions, as proven by Barretta et al. [43] and Vaccaro and Sedighi [44]. Exploiting the stress-driven approach, functionally graded annular nanoplates have been investigated by Jafarinezhad et al. [45], based on the Helmholtz kernel, and by Cianci et al. [46], assuming a Gaussian kernel. The treatment has also been extended to thick plates by Jafarinezhad et al. [47], still assuming an axisymmetric geometry. Following a similar approach, Farajpour et al. [48] obtained a differential formulation for nanoplates of rectangular shape, upon choice of a specific kernel. A simple and effective approach of general validity is here proposed to address elastostatic problems of nanoplates. Notably, the work aims to develop a theoretical formulation and computational procedure for nonlocal elasticity problems. The proposed solution strategy is not limited to plates with particular geometries, boundary and loading conditions, or specific kernels.

Romano et al. [49] introduced iterative methods for solving nonlocal elasticity problems; these methods are general and are not restricted to a specific type of structure. For example, Romano et al. [49] applied the procedure to one-dimensional structures (e.g. Bernoulli–Euler nanobeams), but iterative methods can also be applied to structures defined in higher-dimensional domains. The relevant algorithms require only solutions of standard local elastostatic problems, since the nonlocal solution is obtained by solving a sequence of local problems.

In this work, the iterative method proposed by Romano et al. [49] is implemented for Kirchhoff nanoplates. This approach circumvents the need to introduce constitutive boundary conditions that naturally arise in the analytical differential formulation. Here is the outline. The Kirchhoff theory for elastic plates is first recalled in Section 3 and then the stress-driven nonlocal model is formulated for thin plates. An iterative solution strategy is proposed in Section 4, where the nonlocal response is obtained by iteratively solving a sequence of local problems. In Section 5, the adopted finite element formulation is described along with the numerical integration procedure. Case studies are then examined and solved in Section 6 and concluding remarks are finally provided in Section 7.

3. Kirchhoff theory for local plates and nonlocal nanoplates

The proposed method can be applied to nanoplates of arbitrary geometry. For simplicity, the description refers to the parallelepiped plate shown in Fig. 1, with length, width, and height denoted by L_x, L_y, and t, respectively. The middle plane of the plate is equidistant from the plate surfaces with sides of length L_x and L_y, and is colored gray in Fig. 1. The Cartesian coordinate system has its origin at a vertex of planform of the plate, and the z-axis is oriented upward. The displacements along the x-, y- and z-axes are denoted by u, v, and w, respectively. The rotations around the x- and y-axes are named θ_y and θ_x, respectively, and are such that positive values of these rotations produce negative components u and v for $z > 0$.

Next, the equations of the Kirchhoff plates are briefly recalled. The stress-driven nonlocal integral elasticity is then introduced and applied to Kirchhoff nanoplates (see Tables 1 and 2 for definitions).

3.1. Kinematics

According to the geometrically linearized Kirchhoff theory of plates, kinematics is described by the following relations [50]

$$u = -z\,\theta_x,\ v = -z\,\theta_y, \tag{1}$$

where

$$\theta_x = \frac{\partial w}{\partial x},\ \theta_y = \frac{\partial w}{\partial y}. \tag{2}$$

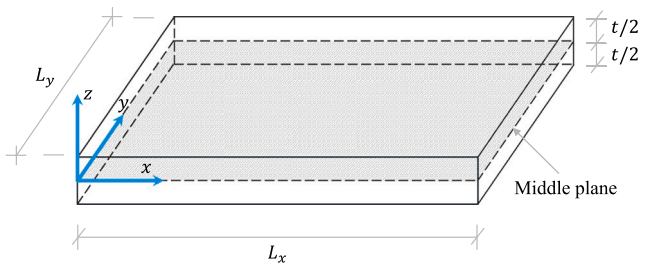

Fig. 1. Geometry of the plate model. (For interpretation of the references to color in this figure legend, the reader is referred to the web version of this article.)

Table 1
Nomenclature for Sections 3, 4, and 6.

Symbol	Meaning
$\mathbb{B}$	Curvature–displacement matrix, $\chi = \mathbb{B}w$
$\boldsymbol{C}$	Material stiffness matrix, $\sigma = \boldsymbol{C}\,\varepsilon^{\mathrm{lc}}$
χ	Total curvature, $\chi = \chi^{\mathrm{el}} + \chi^{\mathrm{in}}$
$\bar{\chi}$	Dimensionless total curvature, $\bar{\chi} = \chi L$
χ^{el}	Elastic curvature, $\chi^{\mathrm{el}} = \chi^{\mathrm{lc}}$ in local analysis, $\chi^{\mathrm{el}} = \chi^{\mathrm{nl}}$ in nonlocal analysis
χ^{in}	Inelastic curvature
χ^{lc}	Elastic local curvature, $\chi^{\mathrm{lc}} = \boldsymbol{D}^{-1}\boldsymbol{M}$
χ^{nl}	Elastic nonlocal curvature, $\chi^{\mathrm{nl}}(x,y) = (\psi * \chi^{\mathrm{lc}})(x,y)$
$\bar{\chi}^{\mathrm{nl}}$	Dimensionless nonlocal curvature, $\bar{\chi}^{\mathrm{nl}} = \chi^{\mathrm{nl}} L$
$\boldsymbol{D}$	Moment–curvature stiffness matrix, $\boldsymbol{D} = t^3\,\boldsymbol{C}/12$
D	Scalar stiffness, $D = \frac{Et^3}{12(1-\nu^2)}$
E	Young's modulus
ε	Strain vector
L	Maximum length of the plate, $L = L_x \geq L_y$
L_c	Length-scale parameter
L_x	Length of the plate along the x-axis
L_y	Length of the plate along the y-axis
λ_x, λ_y	Dimensionless length-scale parameters, $\lambda_x = L_c/L_x$, $\lambda_y = L_c/L_y$
$\boldsymbol{M}$	Moment vector, $\boldsymbol{M} = \boldsymbol{D}\,\chi^{\mathrm{lc}}$
$\bar{\boldsymbol{M}}$	Dimensionless moment vector, $\bar{\boldsymbol{M}} = \boldsymbol{M}L/D$
M_x, M_y	Bending moments
M_{xy}	Twisting moment
n_x, n_y	Number of finite elements along the x- and y-axes
ν	Poisson's ratio
P_{lc}	Local elastostatic operator
ψ	Kernel function
q	Transverse load
$\bar{q}$	Dimensionless transverse load, $\bar{q} = qL^3/D$
$\boldsymbol{r}$	Normalized residual curvature
σ	Stress vector, $\sigma = \boldsymbol{C}\,\varepsilon^{\mathrm{lc}}$
t	Thickness of the plate
θ_x, θ_y	Rotations around the y- and x-axes
u, v	Displacements along the x- and y-axes
w	Transverse displacement (along the z-axis)
$\bar{w}$	Dimensionless transverse displacement, $\bar{w} = w/L$
w^i	Transverse displacement at the ith iteration
w^0	Transverse displacement at iteration 0, i.e. the local displacement
$w_{\max}$	Maximum transverse displacement
$\bar{w}^i, \bar{w}^0, \bar{w}_{\max}$	Dimensionless form of displacements $w^i, w^0, w_{\max}$
x, y, z	Cartesian coordinates
$\bar{x}, \bar{y}$	Dimensionless Cartesian coordinates, $\bar{x} = x/L_x$, $\bar{y} = y/L_y$

The vector collecting the non-zero components of the total tangent deformation is

$$\varepsilon = \begin{Bmatrix} \varepsilon_x \\ \varepsilon_y \\ \gamma_{xy} \end{Bmatrix} = \begin{Bmatrix} \frac{\partial u}{\partial x} \\ \frac{\partial v}{\partial y} \\ \frac{\partial u}{\partial y} + \frac{\partial v}{\partial x} \end{Bmatrix} = \begin{Bmatrix} -z\,\frac{\partial^2 w}{\partial x^2} \\ -z\,\frac{\partial^2 w}{\partial y^2} \\ -2\,z\,\frac{\partial^2 w}{\partial x \partial y} \end{Bmatrix}. \tag{3}$$

Table 2
Nomenclature for Section 5.

Symbol	Meaning
A^e	Area of element e
$\boldsymbol{B}$	Strain–displacement matrix
$\boldsymbol{f}$	Equivalent nodal forces for the whole structure
$\boldsymbol{f}^e$	Equivalent nodal forces of element e
$\boldsymbol{K}$	Global stiffness matrix
$\boldsymbol{K}^e$	Element stiffness matrix
Λ^e	Potential energy of external loads for element e
$\boldsymbol{N}$	Shape functions in the global coordinate system (x, y)
$\hat{\boldsymbol{N}}$	Shape functions in the natural coordinate system (ξ, η)
Φ^e	Strain energy in element e
Π^e	Total potential energy in element e
$\hat{\psi}$	Kernel function in the natural coordinate system (ξ, η)
$\tilde{\boldsymbol{u}}$	Nodal displacements and rotations of the whole structure
$\tilde{\boldsymbol{u}}^e$	Nodal displacements and rotations of element e
V^e	Volume associated to element e
$\tilde{w}$	Transverse displacement evaluated at a node of a finite element
w^e	Transverse displacement of element e
$\tilde{x}_i^e, \tilde{y}_i^e$	Global coordinate of node i of element e

The total curvature vector is defined by

$$\boldsymbol{\chi} = \begin{Bmatrix} \chi_x \\ \chi_y \\ \chi_{xy} \end{Bmatrix} = \begin{Bmatrix} \frac{\partial^2 w}{\partial x^2} \\ \frac{\partial^2 w}{\partial y^2} \\ 2\frac{\partial^2 w}{\partial x \partial y} \end{Bmatrix}, \tag{4}$$

or

$$\boldsymbol{\chi} = \mathbb{B} w, \quad \text{with} \quad \mathbb{B} = \begin{bmatrix} \frac{\partial^2}{\partial x^2} & \frac{\partial^2}{\partial y^2} & 2\frac{\partial^2}{\partial x \partial y} \end{bmatrix}^T. \tag{5}$$

Eqs. (3) and (4) involve the following relationship:

$$\boldsymbol{\varepsilon} = -z\boldsymbol{\chi}. \tag{6}$$

3.2. Equilibrium

The normal bending moments M_x and M_y (for the x and y directions, respectively) and the twisting moment M_{xy} are grouped into the moment vector $\boldsymbol{M}$ and are defined by the following static equivalence

$$\boldsymbol{M} = \begin{Bmatrix} M_x \\ M_y \\ M_{xy} \end{Bmatrix} = -\int_{-t/2}^{t/2} z \begin{Bmatrix} \sigma_x \\ \sigma_y \\ \tau_{xy} \end{Bmatrix} dz, \tag{7}$$

where t is the thickness of the plate; σ_x, σ_y and τ_{xy} are components of the Cauchy stress tensor. The components of $\boldsymbol{M}$ satisfy the following equilibrium equation:

$$\frac{\partial^2 M_x}{\partial x^2} + 2\frac{\partial^2 M_{xy}}{\partial x \partial y} + \frac{\partial^2 M_y}{\partial y^2} = q, \tag{8}$$

where q is the transverse load oriented upward along the z-axis.

3.3. Elastic constitutive laws

In both local and nonlocal elasticity, the constitutive equations correlate the elastic curvature χ^{el} and the moment $\boldsymbol{M}$. In the absence of inelastic strains, the elastic curvature χ^{el} is equal to the total curvature χ, otherwise

$$\chi^{\mathrm{el}} = \chi - \chi^{\mathrm{in}}, \tag{9}$$

where χ^{in} is the inelastic curvature. The strain–curvature relationship for elastic and inelastic fields is given by:

$$\boldsymbol{\varepsilon}^{\mathrm{type}} = -z\,\boldsymbol{\chi}^{\mathrm{type}}, \tag{10}$$

where type = el, in. In the following, the elastic curvature χ^{el} is denoted by χ^{lc} within the local elasticity theory outlined in Section 3.3.1, and by χ^{nl} within the nonlocal integral elasticity theory discussed in Section 3.3.2.

3.3.1. Local elasticity for plates

For a homogeneous isotropic linear elastic material, the local constitutive relationship between stress $\boldsymbol{\sigma}$ and local strain $\boldsymbol{\varepsilon}^{\mathrm{lc}}$ is given by

$$\boldsymbol{\sigma} = \boldsymbol{C}\,\boldsymbol{\varepsilon}^{\mathrm{lc}}, \tag{11}$$

where

$$\boldsymbol{\sigma} = \begin{Bmatrix} \sigma_x \\ \sigma_y \\ \tau_{xy} \end{Bmatrix}, \quad \boldsymbol{C} = \frac{E}{1-\nu^2}\begin{bmatrix} 1 & \nu & 0 \\ \nu & 1 & 0 \\ 0 & 0 & \frac{(1-\nu)}{2} \end{bmatrix}, \quad \boldsymbol{\varepsilon}^{\mathrm{lc}} = \begin{Bmatrix} \varepsilon_x^{\mathrm{lc}} \\ \varepsilon_y^{\mathrm{lc}} \\ \gamma_{xy}^{\mathrm{lc}} \end{Bmatrix}. \tag{12}$$

In Eq. (12), E and ν are Young's modulus and Poisson's ratio, respectively. The local strain $\boldsymbol{\varepsilon}^{\mathrm{lc}}$ can also be expressed in terms of the local curvature χ^{lc}:

$$\boldsymbol{\varepsilon}^{\mathrm{lc}} = -z \begin{Bmatrix} \chi_x^{\mathrm{lc}} \\ \chi_y^{\mathrm{lc}} \\ \chi_{xy}^{\mathrm{lc}} \end{Bmatrix} = -z\,\boldsymbol{\chi}^{\mathrm{lc}}. \tag{13}$$

Taking into account the stress–strain relationship in Eq. (11) and the definitions in Eq. (7), the moment vector is

$$\boldsymbol{M} = \int_{-t/2}^{t/2} z^2\,\boldsymbol{C}\,\boldsymbol{\chi}^{\mathrm{lc}}\,dz = \boldsymbol{D}\,\boldsymbol{\chi}^{\mathrm{lc}}, \tag{14}$$

where

$$\boldsymbol{D} = \frac{t^3}{12}\boldsymbol{C}. \tag{15}$$

Taking into account also Eqs. (5) and (9), the final moment–curvature constitutive relationship is

$$\boldsymbol{M} = \boldsymbol{D}\left(\mathbb{B} w - \boldsymbol{\chi}^{\mathrm{in}}\right). \tag{16}$$

3.3.2. Stress-driven nonlocal integral elasticity for nanoplates

A stress-driven integral approach is adopted as proposed by Romano and Barretta [28], where the nonlocal curvature at a reference point (x, y) in the nanoplate depends not only on the moment at (x, y) but also on the moments at all other points. The curvature according to the nonlocal elasticity approach is denoted by χ^{nl} and is defined as the integral convolution of the moment vector $\boldsymbol{M}$:

$$\begin{aligned} \boldsymbol{\chi}^{\mathrm{nl}}(x,y) = \begin{Bmatrix} \chi_x^{\mathrm{nl}} \\ \chi_y^{\mathrm{nl}} \\ \chi_{xy}^{\mathrm{nl}} \end{Bmatrix} &= \int_A \psi(x-x', y-y', \tau)\,\boldsymbol{D}^{-1}\boldsymbol{M}(x',y')\,dx'dy' \\ &= (\psi * \boldsymbol{D}^{-1}\boldsymbol{M})(x,y) = (\psi * \boldsymbol{\chi}^{\mathrm{lc}})(x,y), \end{aligned} \tag{17}$$

where A is the middle plane area of the nanoplate, ψ is a kernel function [22], and τ is a parameter defined in Appendix A.

The proposed method is not limited to a particular kernel ψ. Therefore, different types of functions ψ are used in Section 6 and explained in Appendix A. Both χ^{lc} and χ^{nl} are elastic curvatures with the difference that χ^{lc} is evaluated by Eq. (14) within a local approach and is equal to $\boldsymbol{D}^{-1}\boldsymbol{M}$, while χ^{nl} is the convolution of the local curvature $\boldsymbol{D}^{-1}\boldsymbol{M}$ in the stress-driven nonlocal integral elasticity.

4. Iterative method for nonlocal elastostatic problems of nanoplates

The mechanical behavior of nanoplates governed by the nonlocal constitutive law in Eq. (17) involves integro-partial differential equations that are generally difficult to solve. For axisymmetric nanoplates,

these equations can be reduced to a set of partial differential equations, as shown by Romano and Barretta [28], and applied by Barretta et al. [43] and Vaccaro and Sedighi [44], upon a specific choice of the kernel. A more general solution procedure is here developed to solve general problems of nanoplates, applicable to arbitrary geometries, boundary and loading conditions, and kernels.

Notably, an iterative method [49] is implemented for Kirchhoff nanoplates. To this end, a local elastostatic operator $P_{\rm lc}$ is defined: this operator determines the transverse displacement w of the local elastic plate (according to the classical plate theory described in Sections 3.1, 3.2, and 3.3.1) subjected to the transverse distributed loading q and the inelastic curvature $\chi^{\rm in}$:

$$w = P_{\rm lc}(q, \chi^{\rm in}). \tag{18}$$

Box 1 describes the steps of the iterative procedure adopted in this work.

Box 1. Iterative method for stress-driven integral elasticity:

Iteration 0. Evaluate the local displacement solution w^0 due to the external transverse distributed load q:

$$w^0 = P_{\rm lc}(q, \chi^{\rm in} = \mathbf{0}). \tag{19}$$

a. Evaluate local curvatures and moments corresponding to w^0:

$$(\chi^{\rm lc})^0 = \mathbb{B}w^0, \quad \boldsymbol{M}^0 = \boldsymbol{D}\mathbb{B}w^0. \tag{20}$$

b. Initialize the total displacement w and the total moment $\boldsymbol{M}$:

$$w = w^0, \quad \boldsymbol{M} = \boldsymbol{M}^0. \tag{21}$$

c. Assign $r = 1$ to enable the starting of the iteration procedure and $i = 0$.

Next iterations. While $r \geq tol$ do:

a. Increment the loop index: $i = i + 1$.

b. Evaluate the nonlocal curvature through Eq. (17):

$$(\chi^{\rm nl})^i(x,y) = (\psi * (\chi^{\rm lc})^{i-1})(x,y). \tag{22}$$

c. Evaluate the residual curvature $\chi^{\rm res}$ at the i-th iteration:

$$(\chi^{\rm res})^i = (\chi^{\rm nl})^i - (\chi^{\rm lc})^{i-1}. \tag{23}$$

d. Solve the plate subjected to the inelastic curvature $(\chi^{\rm in})^i$ equal to the residual $(\chi^{\rm res})^i$:

$$(\chi^{\rm in})^i = (\chi^{\rm res})^i, \quad w^i = P_{\rm lc}(q = 0, (\chi^{\rm in})^i). \tag{24}$$

e. Evaluate the local curvatures and moments corresponding to w^i and $(\chi^{\rm in})^i$:

$$(\chi^{\rm lc})^i = \mathbb{B}w^i - (\chi^{\rm in})^i, \quad \boldsymbol{M}^i = \boldsymbol{D}\left[\mathbb{B}w^i - (\chi^{\rm in})^i\right]. \tag{25}$$

f. Update the total displacement and moment:

$$w = w + w^i, \quad \boldsymbol{M} = \boldsymbol{M} + \boldsymbol{M}^i. \tag{26}$$

g. Calculate the residual r accordingly to Eq. (28).

The procedure reported in Box 1 is based on the sequential solution of linear elastic problems; therefore, the fulfillment of the congruence and equilibrium equations is guaranteed at each iteration of the procedure. On the other hand, the nonlocal constitutive law in Eq. (17) is not satisfied but only approximated with a prescribed level of precision, after a certain number of iterations. Specifically, the iteration process terminates when the components of the normalized residual curvature $\boldsymbol{r}$ become smaller than a given convergence tolerance $tol < 1$. The residual $\boldsymbol{r}$ is

$$\boldsymbol{r} = \begin{Bmatrix} r_x \\ r_y \\ r_{xy} \end{Bmatrix} = \begin{Bmatrix} \frac{\int_A |(\mathbb{B}w)_x - \chi_x^{\rm nl}| dA}{\int_A |(\mathbb{B}w)_x| dA} \\ \frac{\int_A |(\mathbb{B}w)_y - \chi_y^{\rm nl}| dA}{\int_A |(\mathbb{B}w)_y| dA} \\ \frac{\int_A |(\mathbb{B}w)_{xy} - \chi_{xy}^{\rm nl}| dA}{\int_A |(\mathbb{B}w)_{xy}| dA} \end{Bmatrix}. \tag{27}$$

In Eq. (27), $[(\mathbb{B}w)_x, (\mathbb{B}w)_y, (\mathbb{B}w)_{xy}]^{\rm T}$ represents the curvature of the deformed nanoplate and is obtained by deriving the transverse displacement w provided by Eq. (26), i.e. w at the end of the current iteration. $\chi^{\rm nl}$ is evaluated as the convolution in Eq. (17), with the moment vector $\boldsymbol{M}$ provided by Eq. (26), i.e., the moment at the end of the current iteration. The convergence criterion is

$$r = \max(r_x, r_y, r_{xy}) \leq tol. \tag{28}$$

The relation in Eq. (28) guarantees that the nonlocal constitutive law in Eq. (17) is satisfied up to a prescribed level of precision, as controlled by the iterative residual norm. Alternatively, the convergence can be checked using the following residual curvature provided by Eq. (23) in Box 1:

$$\boldsymbol{r} = \begin{Bmatrix} r_x \\ r_y \\ r_{xy} \end{Bmatrix} = \begin{Bmatrix} \frac{\int_A |\chi_x^{\rm res}| dA}{\int_A |(\mathbb{B}w)_x| dA} \\ \frac{\int_A |\chi_y^{\rm res}| dA}{\int_A |(\mathbb{B}w)_y| dA} \\ \frac{\int_A |\chi_{xy}^{\rm res}| dA}{\int_A |(\mathbb{B}w)_{xy}| dA} \end{Bmatrix}. \tag{29}$$

5. Finite element approximate solution

5.1. The local elastostatic operator

The local elastostatic operator $P_{\rm lc}$ is defined in Eq. (18) and used in Box 1: this operator is given by the finite element analysis procedure explained in this section. In the finite element method (FEM), the plate middle-plane domain is subdivided into a finite number of subdomains (called elements). The generic element of the mesh is a quadrilateral with four nodes placed at the vertices. The finite element approximation of the transverse displacement w of the generic element e is

$$w^e(x,y) = \sum_{i=1}^{n} N_i(x,y)\,\tilde{u}_i^e = \boldsymbol{N}(x,y)\,\tilde{\boldsymbol{u}}^e, \tag{30}$$

where

$$\boldsymbol{N} = \left[N_1, N_2, \ldots, N_n\right], \quad \tilde{\boldsymbol{u}}^e = \left[\tilde{u}_1^e, \tilde{u}_2^e, \ldots, \tilde{u}_n^e\right]^{\rm T}. \tag{31}$$

In Eq. (31), N_i is the ith shape function and $\tilde{u}_i^e$ is the ith nodal parameter, i.e., the value that a displacement or rotation (e.g., w, θ_x, or others) assumes at a node of the element. The unknowns of the problem are the nodal parameters grouped in the vector $\tilde{\boldsymbol{u}}^e$. The shape functions N_i also depend on the element e, but the superscript e on the symbol N_i and on other objects referring to the element e is omitted for brevity. Appendices B and C present the shape functions corresponding to two different finite elements used in the numerical simulations of this study. Specifically, the Melosh–Zienkiewicz–Cheung (MZC) element is briefly recalled in Appendix B, while the Bogner–Fox–Schmit (BFS) element is referenced in Appendix C.

The strain vector is

$$\boldsymbol{\varepsilon} = \begin{Bmatrix} \varepsilon_x \\ \varepsilon_y \\ \gamma_{xy} \end{Bmatrix} = -z\,\mathbb{B}w^e = -z\,\boldsymbol{B}\tilde{\boldsymbol{u}}^e, \tag{32}$$

where

$$\boldsymbol{B} = \mathbb{B}\boldsymbol{N} = \begin{bmatrix} \mathbb{B}N_1 & \mathbb{B}N_2 & \dots & \mathbb{B}N_n \end{bmatrix} = \begin{bmatrix} \frac{\partial^2 N_1}{\partial x^2} & \frac{\partial^2 N_2}{\partial x^2} & \dots & \frac{\partial^2 N_n}{\partial x^2} \\ \frac{\partial^2 N_1}{\partial y^2} & \frac{\partial^2 N_2}{\partial y^2} & \dots & \frac{\partial^2 N_n}{\partial y^2} \\ 2\frac{\partial^2 N_1}{\partial x \partial y} & 2\frac{\partial^2 N_2}{\partial x \partial y} & \dots & 2\frac{\partial^2 N_n}{\partial x \partial y} \end{bmatrix} \tag{33}$$

The total potential energy (TPE) of the e-element is given by

$$\Pi^e = \Phi^e + \Lambda^e, \tag{34}$$

where Φ^e is the strain energy associated with bending and twisting deformations

$$\Phi^e = \frac{1}{2}\int_{V_e} \left(\boldsymbol{\varepsilon}^{\mathrm{lc}}\right)^{\mathrm{T}} \boldsymbol{C}\boldsymbol{\varepsilon}^{\mathrm{lc}}\, dV = \frac{1}{2}\int_{V_e} \left(\boldsymbol{\varepsilon} - \boldsymbol{\varepsilon}^{\mathrm{in}}\right)^{\mathrm{T}} \boldsymbol{C}\left(\boldsymbol{\varepsilon} - \boldsymbol{\varepsilon}^{\mathrm{in}}\right) dV, \tag{35}$$

and Λ^e is the opposite of the external work:

$$\Lambda^e = -\int_{A_e} w^e\, q\, dA = -\int_{A_e} (\tilde{\boldsymbol{u}}^e)^{\mathrm{T}}\, \boldsymbol{N}^{\mathrm{T}} q\, dA. \tag{36}$$

In Eqs. (35) and (36), V_e is the volume corresponding to element e and A_e is the area of element e. Taking into account Eqs. (10), (15) and (32), the strain energy is

$$\begin{aligned} \Phi^e &= \frac{1}{2}\int_{-t/2}^{t/2} z^2 \int_{A_e} \left(\boldsymbol{B}\tilde{\boldsymbol{u}}^e - \boldsymbol{\chi}^{\mathrm{in}}\right)^{\mathrm{T}} \boldsymbol{C}\left(\boldsymbol{B}\tilde{\boldsymbol{u}}^e - \boldsymbol{\chi}^{\mathrm{in}}\right) dA\, dz \\ &= \frac{1}{2}\int_{A_e} \left[(\tilde{\boldsymbol{u}}^e)^{\mathrm{T}}\, \boldsymbol{B}^{\mathrm{T}}\left(\boldsymbol{D}\boldsymbol{B}\tilde{\boldsymbol{u}}^e - 2\boldsymbol{D}\boldsymbol{\chi}^{\mathrm{in}}\right) + \left(\boldsymbol{\chi}^{\mathrm{in}}\right)^{\mathrm{T}} \boldsymbol{D}\boldsymbol{\chi}^{\mathrm{in}}\right] dA. \end{aligned} \tag{37}$$

Applying the principle of minimum total potential energy provides the following equilibrium equation of element e:

$$\boldsymbol{K}^e\tilde{\boldsymbol{u}}^e = \boldsymbol{f}^e, \tag{38}$$

where the element stiffness matrix $\boldsymbol{K}^e$ and the equivalent nodal forces $\boldsymbol{f}^e$ for the generic element e are given by

$$\begin{aligned} \boldsymbol{K}^e &= \int_{A_e} \boldsymbol{B}^{\mathrm{T}}\boldsymbol{D}\boldsymbol{B}\, dA, \\ \boldsymbol{f}^e &= \int_{A_e} \boldsymbol{B}^{\mathrm{T}}\boldsymbol{D}\boldsymbol{\chi}^{\mathrm{in}}\, dA + \int_{A_e} \boldsymbol{N}^{\mathrm{T}} q\, dA. \end{aligned} \tag{39}$$

The global system of equations

$$\boldsymbol{K}\tilde{\boldsymbol{u}} = \boldsymbol{f} \tag{40}$$

is obtained by assembling the element stiffness matrices and equivalent nodal forces. The solution $\tilde{\boldsymbol{u}}$ of Eq. (40) provides, after post-processing, the unknown displacement w due to:

- the transverse load q,
- the inelastic curvature $\boldsymbol{\chi}^{\mathrm{in}}$.

This gives the operator P_{lc} in Eq. (18).

The integrals in Eqs. (17) and (39) are evaluated with Gaussian quadrature. First, the integral over A_e is converted to an integral over the square domain defined by $-1 \leqslant \xi, \eta \leqslant 1$. To this end, the square element defined in the natural coordinate system (ξ, η) is transformed into the element e defined in the global coordinate system (x, y) via the following parametric mapping

$$\begin{cases} x(\xi,\eta) = \sum_{i=1}^{4} \hat{N}_i(\xi,\eta)\, \tilde{x}_i^e, \\ y(\xi,\eta) = \sum_{i=1}^{4} \hat{N}_i(\xi,\eta)\, \tilde{y}_i^e, \end{cases} \tag{41}$$

where $\hat{N}_1, \dots, \hat{N}_4$ are bilinear shape functions reported in Appendix D and $(\tilde{x}_i^e, \tilde{y}_i^e)$ are the (x, y) coordinates of node i of element e. The integral of a generic function $g = g(x, y)$ over A_e is evaluated as

$$\begin{aligned} \int_{A_e} g(x,y)dx\, dy &= \int_{-1}^{1}\int_{-1}^{1} \hat{g}(\xi,\eta)J(\xi,\eta)d\xi\, d\eta \\ &= \sum_{i=1}^{n_1}\sum_{j=1}^{n_2} \hat{g}(\xi_i,\eta_j)J(\xi_i,\eta_j)W_{ij}, \end{aligned} \tag{42}$$

where

$$\hat{g}(\xi,\eta) = g(x(\xi,\eta), y(\xi,\eta)), \tag{43}$$

$J(\xi, \eta)$ is the Jacobian of the transformation in Eq. (41), (ξ_i, η_j) is a Gauss point and W_{ij} is the weight associated with the Gauss point (ξ_i, η_j). Given a function $g = g(x, y)$, the symbol $\hat{g}$ will denote the composition of functions represented in Eq. (43).

5.2. Evaluating the nonlocal curvature through the FEM integral convolution

Before evaluating the nonlocal curvature (17), it is necessary to determine the following moment vector $\hat{\boldsymbol{M}}^k$ at the Gauss point (ξ_l, η_m) of the element k

$$\hat{\boldsymbol{M}}^k(\xi_l,\eta_m) = \boldsymbol{D}\left(\hat{\boldsymbol{\chi}}^{\mathrm{lc}}\right)^k(\xi_l,\eta_m) = \boldsymbol{D}\left[\hat{\boldsymbol{B}}(\xi_l,\eta_m)\tilde{\boldsymbol{u}}^k - \left(\hat{\boldsymbol{\chi}}^{\mathrm{in}}\right)^k(\xi_l,\eta_m)\right]. \tag{44}$$

Then, the convolution in Eq. (17) is numerically evaluated using the Gauss quadrature, integrating over the total number n_e of the mesh elements: the nonlocal curvature $\left(\hat{\boldsymbol{\chi}}^{\mathrm{nl}}\right)^e$ at the Gauss point (ξ_i, η_j) of element e is given by

$$\left(\hat{\boldsymbol{\chi}}^{\mathrm{nl}}\right)^e(\xi_i,\eta_j) = \sum_{k=1}^{n_e}\sum_{l=1}^{n_1}\sum_{m=1}^{n_2} \hat{\psi}\, \boldsymbol{D}^{-1}\hat{\boldsymbol{M}}^k(\xi_l,\eta_m)J^k(\xi_l,\eta_m)W_{lm}, \tag{45}$$

where

$$\hat{\psi} = \hat{\psi}(x^e(\xi_i,\eta_j) - x^k(\xi_l,\eta_m), y^e(\xi_i,\eta_j) - y^k(\xi_l,\eta_m), \tau), \tag{46}$$

and $\left(x^e(\xi_i,\eta_j), y^e(\xi_i,\eta_j)\right)$ are the global coordinates corresponding to the Gauss point with natural coordinates (ξ_i, η_j) through the transformation in Eq. (41). The same holds for the coordinates $\left(x^k(\xi_l,\eta_m), y^k(\xi_l,\eta_m)\right)$.

The most CPU time-consuming operations in the algorithms reported in Box 1 are:

1. the determination of the elastostatic local solution through the operator P_{lc};
2. the evaluation of the nonlocal generalized strains $\hat{\boldsymbol{\chi}}^{\mathrm{nl}}$ through Eq. (45).

6. Case studies

Next, the proposed iterative method is applied to determine the static state of nonlocal nanoplates with different types of boundary conditions. The middle plane of the nanoplates under consideration is rectangular and discretized using rectangular BFS finite elements. Each element of the mesh has side lengths $a_x = L_x/n_x$ and $a_y = L_y/n_y$ along the x- and y-axes, respectively. The parameters n_x and n_y denote the number of finite elements along the x- and y-axes, respectively, see, e.g., Fig. 2. BFS finite elements are adopted in the present analyses because of their superior performance compared to MZC elements.

The presented applications refer to the following types of nanoplates:

- Clamped nanoplates. This type of nanoplate, denoted by the acronym CCCC, has all edges clamped and is characterized by the following boundary conditions (BCs):

$$\begin{cases} w = \dfrac{\partial w}{\partial y} = 0 & \text{for } y = 0, L_y, \\ w = \dfrac{\partial w}{\partial x} = 0 & \text{for } x = 0, L_x. \end{cases} \tag{47}$$

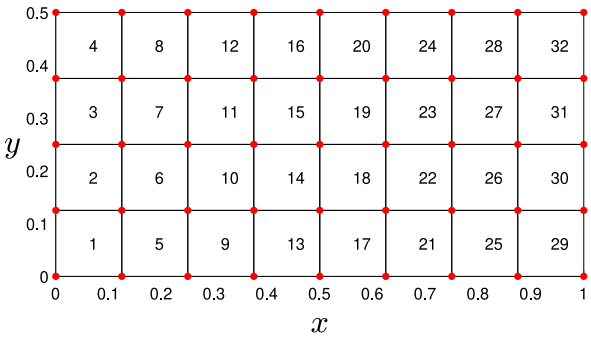

Fig. 2. A finite element mesh with $n_x = 8$ and $n_y = 4$.

- Simply supported nanoplates. Identified by the acronym SSSS, this type of nanoplate exhibits simply supported edges and the BCs are defined as follows:

$$w = 0 \quad \text{for} \begin{cases} y = 0, L_y, \\ x = 0, L_x. \end{cases} \tag{48}$$

- Nanoplates clamped at the edges parallel to the y-axis and free at the other edges; this type of nanoplate, denoted by the acronym FCFC, is characterized by the following BCs:

$$w = \frac{\partial w}{\partial x} = 0 \quad \text{for } x = 0, L_x. \tag{49}$$

- Nanoplates simply supported at the edges parallel to the y-axis and free at the other edges; this type of nanoplate, denoted by the acronym FSFS, is characterized by the following BCs:

$$w = 0 \quad \text{for } x = 0, L_x. \tag{50}$$

The boundary conditions described above require the nodal parameters to satisfy specific constraints, which depend on the type of finite element employed. More details are provided in Appendix E.

All considered nanoplates are subject to a uniformly distributed transverse load q. External moments and shear forces are not applied along the edges of the nanoplates. The results are presented in nondimensional form by defining the following variables:

$$\bar{x} = \frac{x}{L_x}, \ \bar{y} = \frac{y}{L_y}, \ \lambda_x = \frac{L_c}{L_x}, \ \lambda_y = \frac{L_c}{L_y}, \ \bar{q} = \frac{qL^3}{D}, \ \bar{w} = \frac{w}{L}, \\ \bar{\boldsymbol{\chi}} = \boldsymbol{\chi} L, \ \bar{\boldsymbol{M}} = \frac{\boldsymbol{M} L}{D}, \tag{51}$$

where L_c is a length-scale parameter defined in Appendix A and

$$L = L_x \geq L_y, \ D = \frac{Et^3}{12(1-\nu^2)}. \tag{52}$$

The following numerical results show the influence of λ_x, λ_y, and the ratio L_y/L_x on the deflection of the nanoplates.

6.1. One-dimensional case: cylindrical bending

This first example considers the cylindrical bending of nanoplates: the variables of the problem do not depend on y. The only non-zero components of $\bar{\boldsymbol{M}}$ and $\bar{\boldsymbol{\chi}}$ are $\bar{M}_x$ and $\bar{\chi}_x$, respectively. To this end, it is assumed $\nu = 0$, to avoid the formation of curvatures $\bar{\chi}_y$ and $\bar{\chi}_{xy}$, see, e.g., Fig. 3. The following non-dimensional nonlocal constitutive law is adopted:

$$\bar{\chi}^{\text{nl}}(\bar{x}) = \frac{1}{2\lambda_x} \int_0^1 \exp\left(-\frac{|\bar{x} - \bar{x}'|}{\lambda_x}\right) \bar{\boldsymbol{M}}(\bar{x}') \, d\bar{x}' \tag{53}$$

where the one-dimensional kernel function (A.1) reported in Appendix A is well recognizable. The boundary conditions must also be independent of y. Therefore, FCFC and FSFS nanoplates are considered next.

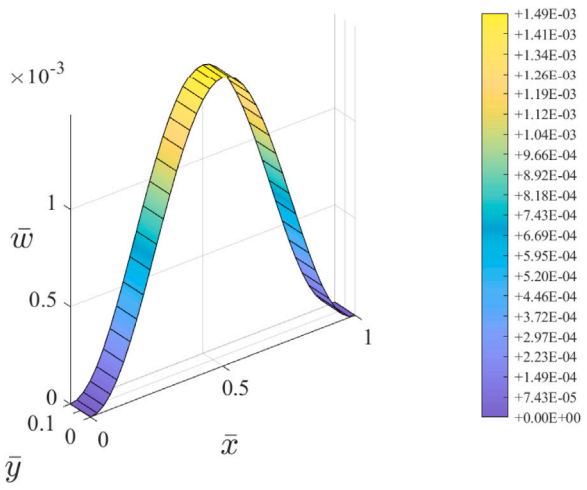

Fig. 3. Dimensionless transverse displacement $\bar{w}$ for the FCFC nanoplate characterized by $\lambda_x = 0.1$ and $\bar{q} = 1$ in cylindrical bending.

Clearly, the nanostructures considered here with nonlocal curvature in Eq. (53) behave like nonlocal nanobeams, for which exact closed-form solutions are available. However, the main objective of this section is not only to validate the method but also to highlight the distinctive features of the proposed iterative method within the framework of stress-driven nonlocal integral elasticity.

In Fig. 4, the dimensionless transverse displacement $\bar{w}^i = w^i/L$, with $i = 0, 1, 2$, is plotted against $\bar{x}$ for the FCFC nanoplate characterized by $\lambda_x = 0.1$ and $\bar{q} = 1$. In the one-dimensional case under consideration, the use of 2×1 Gauss points is computationally more efficient; however, a 2×2 integration scheme is adopted to ensure consistency and ease of implementation. The number of finite elements along the x- and y-axes is $n_x = 40$ and $n_y = 1$, respectively. From Box 1, w^i/L is the dimensionless transverse displacement at the ith iteration and must tend to the exact dimensionless displacement $\bar{w}^{\text{exact}}$ as i tends to ∞. Observing the analogy between the cylindrical bending of nanoplates and the one-dimensional bending of nanobeams, $\bar{w}^{\text{exact}}$ is the solution of the following sixth-order differential equation, which governs the nonlocal behavior of nanobeams:

$$\frac{d^6\bar{w}}{d\bar{x}^6} - \frac{1}{\lambda_x^2}\frac{d^4\bar{w}}{d\bar{x}^4} = -\frac{\bar{q}}{\lambda_x^2}, \tag{54}$$

accompanied by the following constitutive boundary conditions

$$\begin{cases} \left.\dfrac{d^3\bar{w}}{d\bar{x}^3}\right|_{\bar{x}=0} - \dfrac{1}{\lambda_x}\left.\dfrac{d^2\bar{w}}{d\bar{x}^2}\right|_{\bar{x}=0} = 0 \\ \left.\dfrac{d^3\bar{w}}{d\bar{x}^3}\right|_{\bar{x}=1} + \dfrac{1}{\lambda_x}\left.\dfrac{d^2\bar{w}}{d\bar{x}^2}\right|_{\bar{x}=1} = 0. \end{cases} \tag{55}$$

The approximate numerical solution $\bar{w}^i$ is practically indistinguishable from the exact solution $\bar{w}^{\text{exact}}$ for $i = 2$. The same fast convergence is not expected to occur in the cases of Section 6.2. Surprisingly, the two-dimensional nanoplates of Section 6.2, characterized by a more complex distribution of moments and curvatures, will show fast convergence, again, in the presence of CCCC BCs and small λ_x.

Increasing the number of Gauss points slightly improves the accuracy of the numerical solution, as shown in Fig. 5, where the solutions obtained using 2×2 and 3×3 Gauss quadrature schemes are compared in the central region of the nanostructure, which is shown in a magnified view focusing exclusively on this area.

A distinctive feature of the proposed FEM-based iterative procedure is the dependence of the mesh density on the length-scale parameter λ_x

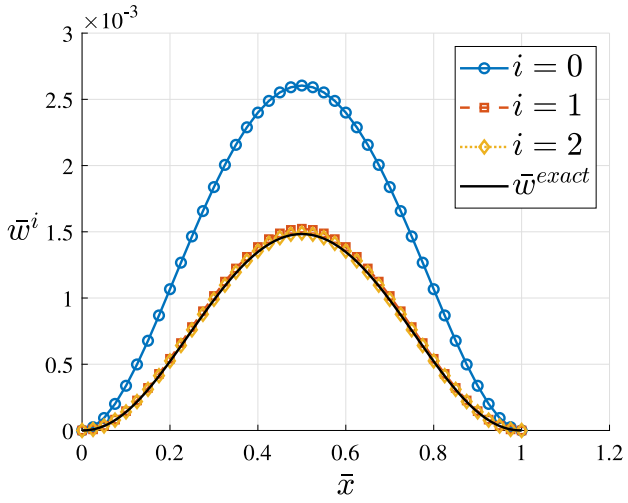

(a)

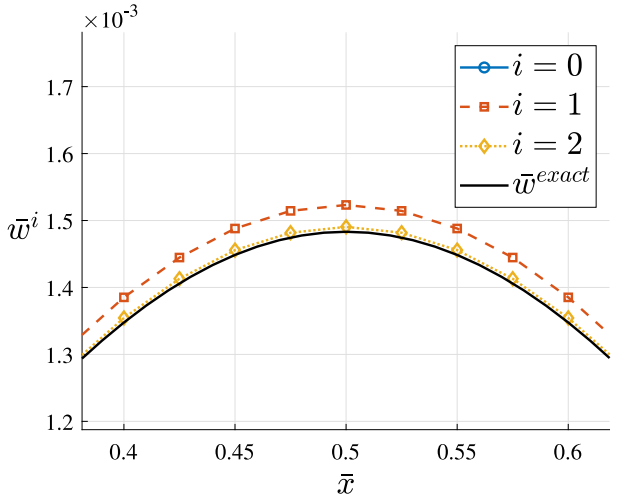

(b)

Fig. 4. (a) Dimensionless transverse displacement $\bar{w}^i$, with $i = 0, 1, 2$, plotted against $\bar{x}$ for the FCFC nanoplate characterized by $\lambda_x = 0.1$ and $\bar{q} = 1$ in cylindrical bending; (b) a magnified view of Fig. 4a.

(or the characteristic length L_c), where the mesh density is defined as the number of planar finite elements per unit area. The kernel function ψ introduced in Section 3.3.2 is a delta sequence, i.e. ψ converges to the Dirac delta function as L_c tends to zero, see Appendix A. As a consequence, the integrand in Eq. (17) varies significantly over the integration domain, represented by the middle plane of the nanoplate. The domain of integration is divided into $n_x \times n_y$ subdomains, where each subdomain is a finite element area. In the presence of smaller values of L_c, an accurate integration requires a smaller subdomain of integration, that is, smaller dimensions of finite elements. In the one-dimensional case considered in this section, the finite element dimension $a_x = L_x/n_x$ along the x-axis should decrease as the length-scale parameter $\lambda_x = L_c/L$ decreases, involving an inverse relationship between n_x and λ_x.

The influence of n_x and the mesh density on the convergence of $\bar{w}^i$ as $i \to \infty$ is shown in Figs. 6 and 7, where the maximum dimensionless displacement $\bar{w}^i_{\max}$ (given by $\bar{w}^i$ evaluated at abscissa $\bar{x} = 0.5$) is plotted against the iteration index i for different values of the number n_x of finite elements along the x-axis. Figs. 6 and 7 refer to FCFC nanoplates subjected to $\bar{q} = 1$ with discretization characterized by 2×2 Gauss points and $n_y = 1$. In Fig. 6, the length-scale parameter λ_x is equal

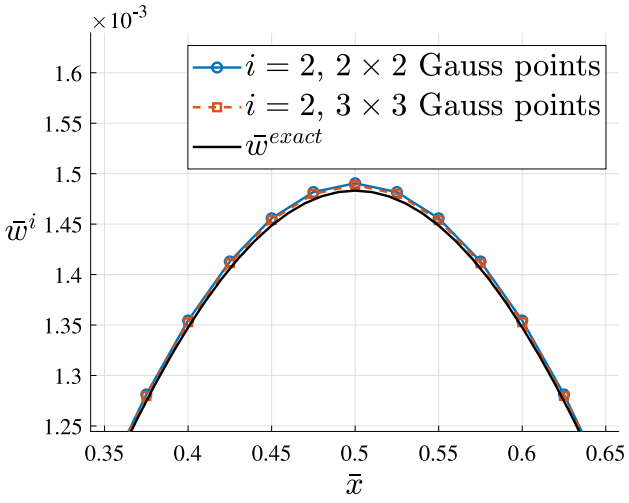

Fig. 5. Accuracy increasing with the number of Gauss points for the FCFC nanoplate characterized by $\lambda_x = 0.1$ and $\bar{q} = 1$ in cylindrical bending; only the central region of the nanostructure is shown in a magnified view focusing exclusively on this area.

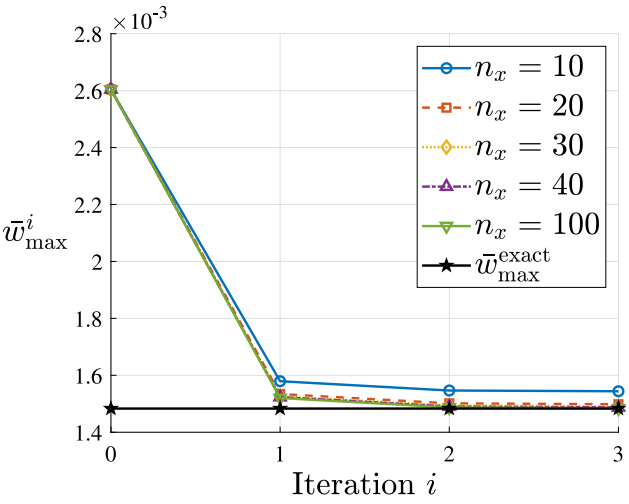

Fig. 6. Maximum dimensionless displacement $\bar{w}^i_{\max} = \bar{w}^i(0.5)$ plotted against the iteration index i for different values of the number n_x of finite elements along the x-axis (FCFC nanoplate with $\lambda_x = 0.1$ and $\bar{q} = 1$ in cylindrical bending).

to 0.1 and the piecewise linear curve corresponding to $n_x = 10$ is far from the curve referring to $n_x = 20$, showing a mesh sensitivity for the adopted length-scale parameter. On the other hand, the same curves in Fig. 7, obtained by assuming a larger parameter $\lambda_x = 0.2$, are very close: a coarse mesh with $n_x = 10$ almost gives the same accuracy as fine meshes with $n_x = 20, 30, 40, 100$. From the examples in Figs. 6 and 7, it appears that the value $n_x = 2/\lambda_x$ provides acceptable results.

In statically determinate structures, the adopted iterative method converges to the exact solution after the first iteration. This is shown in Fig. 8, where the dimensionless displacement $\bar{w}^i$, with $i = 0, 1$, is plotted against $\bar{x}$ for the FSFS nanoplate characterized by $\lambda_x = 0.1$ and $\bar{q} = 1$; the mesh is defined by $n_x = 40$ and $n_y = 1$, with 2×2 Gauss points.

6.2. Two-dimensional analyses

In this section, the Poisson's ratio ν is greater than zero (and taken equal to 0.3) so that both curvatures $\bar{\chi}_x$ and $\bar{\chi}_y$ are different from zero.

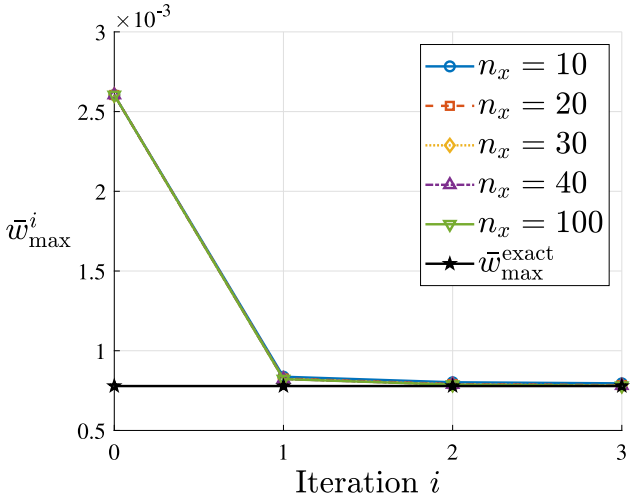

Fig. 7. Maximum dimensionless displacement $\bar{w}^i_{\max} = \bar{w}^i(0.5)$ plotted against the iteration index i for different values of the number n_x of finite elements along the x-axis (FCFC nanoplate with $\lambda_x = 0.2$ and $\bar{q} = 1$ in cylindrical bending).

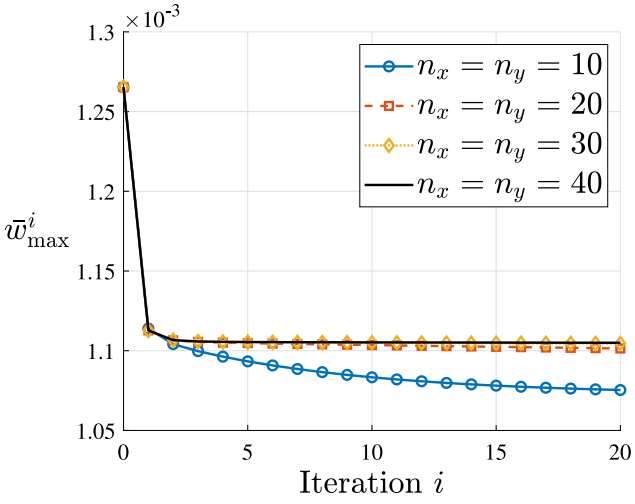

Fig. 9. Maximum dimensionless displacement $\bar{w}^i_{\max} = \bar{w}^i(0.5, 0.5)$ plotted against the iteration index i for different mesh densities (CCCC square nanoplate with $\lambda_x = 0.05$ and $\bar{q} = 1$).

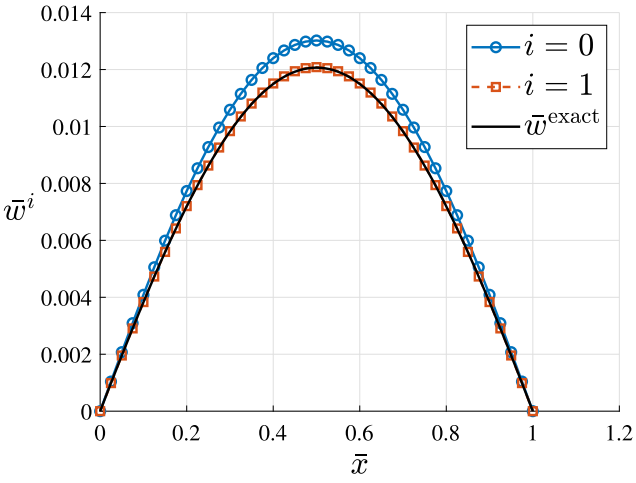

Fig. 8. Dimensionless transverse displacement $\bar{w}^i$, with $i = 0, 1$, plotted against $\bar{x}$ for the FSFS nanoplate characterized by $\lambda_x = 0.1$ and $\bar{q} = 1$ in cylindrical bending.

Unless otherwise stated, the kernel function (A.3) in Appendix A is adopted and numerical integration is carried out using a 3×3 Gauss quadrature scheme.

In nonlocal analyses, particular attention must be given to the characteristics of the finite element model, such as mesh density and Gauss point configuration, as their influence is significantly more pronounced than in local analyses. This observation is supported by the data presented in Fig. 9, where the maximum dimensionless displacement $\bar{w}^i_{\max}$ is plotted against the iteration index i for different mesh densities. The figure refers to the CCCC square nanoplate with $\lambda_x = 0.05$ and $\bar{q} = 1$. The maximum dimensionless displacement $\bar{w}^i_{\max}$ is given by $\bar{w}^i$ evaluated at the center point $(\bar{x}, \bar{y}) = (0.5, 0.5)$ of the middle plane of the nanoplate. The mesh density can be represented by the product $n_x \times n_y$, where n_x and n_y are the number of finite elements along the x- and y-axes, respectively. The local solution is given by $\bar{w}^0$, that is, the dimensionless displacement $\bar{w}$ at the initial iteration 0, and it remains unchanged regardless of the finite element mesh adopted. In contrast, nonlocal approximations $\bar{w}^i$, for $i > 0$, are influenced by the mesh density. In other words, the meshes with $n_x = n_y = 10, 20$ yield sufficiently accurate results in the local analysis, whereas they prove inadequate for the nonlocal analysis due to their excessively coarse resolution. Fig. 9 also shows that the mesh with $n_x = n_y = 30$ provides quite accurate results similar to those given by the fine mesh with $n_x = n_y = 40$.

As discussed in Section 6.1, the appropriate mesh density is influenced by the length-scale parameter $\lambda_x = L_c/L$. This influence also holds in the two-dimensional analyses presented in this section. Given that the kernel function ψ, introduced in Section 3.3.2, constitutes a delta sequence, the integrand in Eq. (17) varies significantly over the integration domain for smaller values of λ_x, requiring a more accurate integration through mesh refinement. The influence of the mesh density on the convergence of $\bar{w}^i$ as $i \to \infty$ can be understood by comparing Figs. 9 and 10. In both figures, the maximum dimensionless displacement $\bar{w}^i_{\max}$ is plotted against the iteration index i for different mesh densities in CCCC square nanoplates subjected to $\bar{q} = 1$. In Fig. 9, the length-scale parameter λ_x is equal to 0.05 and the piecewise linear curve corresponding to $n_x = n_y = 20$ is far from the curve referring to $n_x = n_y = 30$, showing a mesh sensitivity for the adopted length-scale parameter. On the other hand, the same curves in Fig. 10, obtained by assuming a larger parameter $\lambda_x = 0.15$, are very close: a coarse mesh with $n_x = n_y = 20$ almost gives the same accuracy as fine meshes with $n_x = n_y = 30, 40$.

In Fig. 10, the mesh with $n_x = 10$ deserves particular attention: initially, it provides results of acceptable accuracy; however, for iterations $i > 20$, the corresponding curve slightly deviates from the other curves. Apparently, the choice $n_x = n_y = 2/\lambda_x$ yields satisfactory results for the square nanoplates examined above, consistent with the value $n_x = 2/\lambda_x$ adopted in the cylindrical bending case discussed in Section 6.1. In reality, the rule $n_x = n_y = 2/\lambda_x$ may yield inadequate results, particularly observable after a large number of iterations. To avoid adopting an inadequate mesh, it is useful to examine the convergence behavior over a relatively large number of iterations.

At first glance, larger values of the parameter λ_x may appear to reduce computational costs, as coarser meshes yield results of acceptable accuracy. However, increasing λ_x amplifies nonlocal effects due to weaker attenuation induced by the kernel function. Consequently, a larger number of iterations is required to meet the convergence criterion in Eq. (28), which ensures that the normalized residual curvature falls below a prescribed tolerance. This observation arises from analyzing the slopes of the curves in Figs. 9 and 10. In Fig. 9 ($\lambda_x = 0.05$), the slopes become nearly zero after the tenth iteration. In contrast, in

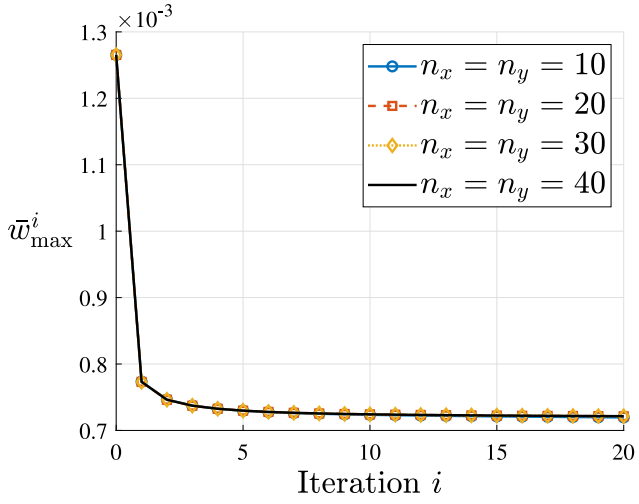

Fig. 10. Maximum dimensionless displacement $\bar{w}^i_{\max} = \bar{w}^i(0.5, 0.5)$ plotted against the iteration index i for different mesh densities (CCCC square nanoplate with $\lambda_x = 0.15$ and $\bar{q} = 1$).

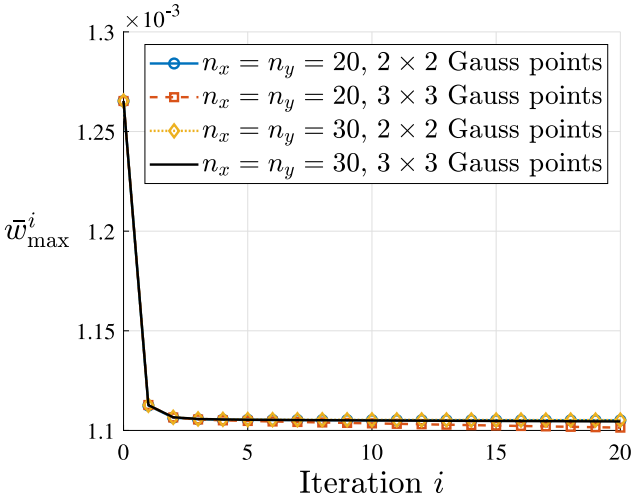

Fig. 11. Maximum dimensionless displacement $\bar{w}^i_{\max} = \bar{w}^i(0.5, 0.5)$ plotted against the iteration index i for different mesh densities and two types of Gaussian quadrature (CCCC square nanoplate with $\lambda_x = 0.05$ and $\bar{q} = 1$).

Fig. 10 ($\lambda_x = 0.15$), more than twenty iterations are required before the slopes can be considered negligible. A higher number of iterations is also required to achieve convergence when the boundary constraints of the nanoplate are relaxed, as in the case of simply supported nanoplates (SSSS).

The influence of Gaussian quadrature on nonlocal solutions is more accentuated in coarser meshes, as illustrated in Fig. 11, which shows the maximum dimensionless displacement $\bar{w}^i_{\max} = \bar{w}^i(0.5, 0.5)$ plotted against the iteration index i for different mesh densities and two types of Gaussian quadrature, namely 2×2 and 3×3 Gauss point integration. The nanoplate under consideration is square-shaped, subject to fully clamped boundary conditions (CCCC), and characterized by $\lambda_x = 0.05$ and $\bar{q} = 1$. In the figure, there are two piecewise linear curves corresponding to the coarse mesh ($n_x = n_y = 20$): one refers to 2×2 Gauss point integration and the other to 3×3 integration. The two curves are quite far from each other. In contrast, the two piecewise linear curves corresponding to the finer mesh ($n_x = n_y = 30$) are very close. The curve of the mesh with $n_x = n_y = 20$ and 2×2 Gauss points is observed to coincide with the curves of the finer mesh characterized by $n_x = n_y = 30$. This circumstance does not appear to be fortuitous: 2×2 Gauss quadrature may yield better results than 3×3 Gauss quadrature when the kernel in Eq. (A.3) is used and the meshes are relatively coarse. However, numerical simulations based on the kernel in Eq. (A.2) exhibit standard behavior, with 3×3 Gauss quadrature providing greater accuracy than 2×2 Gauss quadrature.

In the considered analyses, the mesh density and the Gauss point configuration significantly influence the nonlocal results, while their impact on the local solution is negligible.

In Fig. 12, the normalized residual curvatures r_x and r_{xy} in Eq. (27) are plotted against the iteration i for the CCCC square nanoplate with $\lambda_x = 0.05$, $\bar{q} = 1$, and mesh characterized by $n_x = n_y = 30$. It is observed that while the residual r_{xy} decreases with increasing iteration index i, the residual r_x remains nearly constant beyond the fifth iteration. This indicates that the accuracy of the iterative solution has reached its limit for the current discretization. A further reduction of r_x can only be achieved by increasing the number of finite elements, with mesh refinement. In Fig. 12, the ratio $r_w = \left| \left(\bar{w}^i_{\max} - \bar{w}^{i-1}_{\max} \right) / \bar{w}^0_{\max} \right|$ is also plotted as a function of the iteration index i. The trend of r_w is similar to that of r_x. Furthermore, after the fifth iteration, the ratio is practically equal to zero, indicating that the dimensionless displacement remains constant. In Fig. 13, the normalized residual curvatures are plotted against the iteration i for the CCCC square nanoplate with

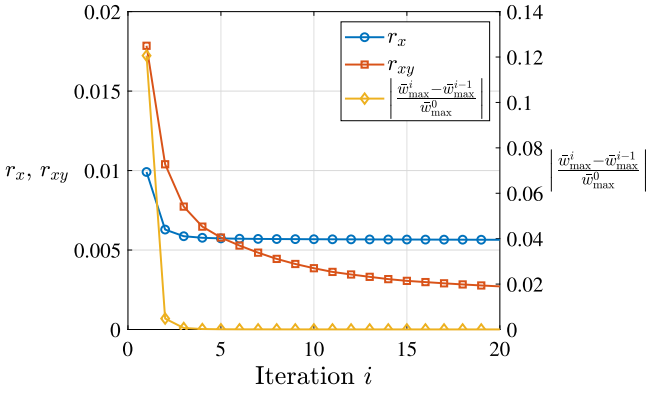

Fig. 12. Normalized residual curvatures r_x and r_{xy} plotted against the iteration index i for the CCCC square nanoplate with $\lambda_x = 0.05$, $\bar{q} = 1$, and $n_x = n_y = 30$.

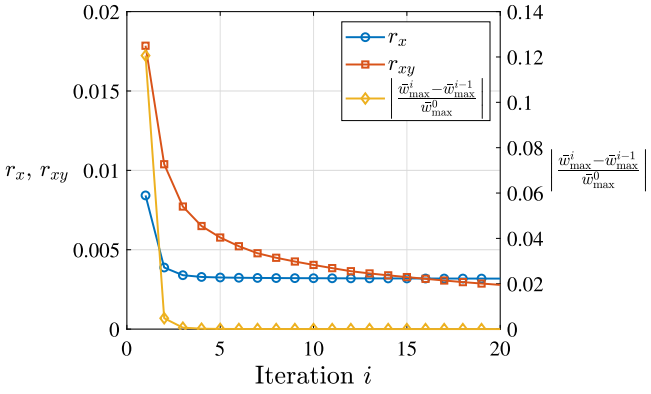

Fig. 13. Normalized residual curvatures r_x and r_{xy} plotted against the iteration index i for the CCCC square nanoplate with $\lambda_x = 0.05$, $\bar{q} = 1$, and $n_x = n_y = 40$.

$\lambda_x = 0.05$, $\bar{q} = 1$, and $n_x = n_y = 40$. The residual curvature r_x in Fig. 12 (mesh with $n_x = n_y = 30$) is larger than r_x in Fig. 13 (mesh with $n_x = n_y = 40$), illustrating the reduction of r_x as the number of finite elements increases with mesh refinement. The dimensionless displacements corresponding to these case studies are shown in Fig. 9.

The stress-driven integral elasticity involves a stiffening effect: nonlocal nanoplates exhibit smaller displacements than those of local

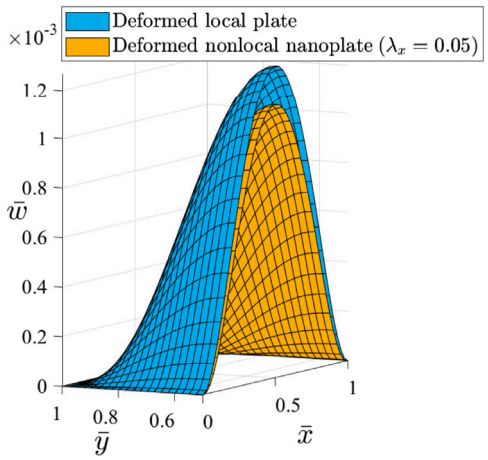

Fig. 14. Deformed configurations of CCCC local and nonlocal square plates subjected to $\bar{q} = 1$.

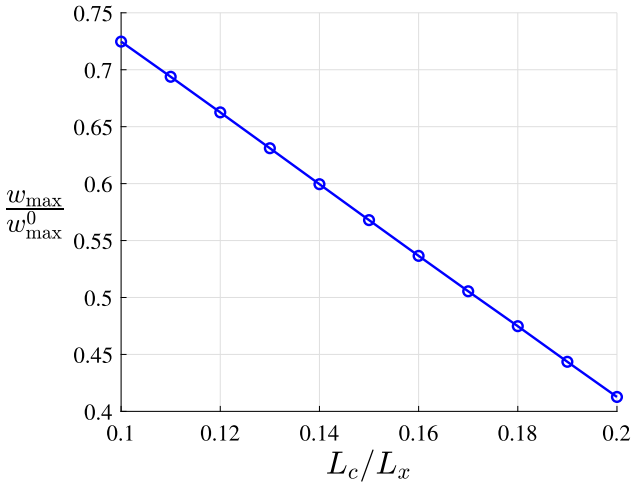

Fig. 15. The ratio $w_{\max}/w^0_{\max}$ plotted against $\lambda_x = L_c/L_x$ for CCCC square nanoplates subjected to $\bar{q} = 1$.

plates. This is shown in Fig. 14, where the deformed configurations of CCCC local and nonlocal square plates subjected to $\bar{q} = 1$ are compared. In Fig. 14, the deformed local plate and nonlocal nanoplate are the graphs of the dimensionless displacement $\bar{w}^i = \bar{w}^i(\bar{x}, \bar{y})$, with $i = 0$ (initial iteration) for the local case and $i = 40$ for the nonlocal case. A fine mesh with $n_x = n_y = 40$ is adopted and λ_x is equal to 0.05 for the nonlocal nanoplate.

More specifically, the nonlocal displacement decreases as the parameter λ_x increases. In Fig. 15, the ratio $w_{\max}/w^0_{\max}$ is plotted against λ_x for CCCC square nanoplates subjected to $\bar{q} = 1$. $w_{\max}$ and $w^0_{\max}$ are the nonlocal and local displacements, respectively, evaluated at the center point $(\bar{x}, \bar{y}) = (0.5, 0.5)$ of the nanoplates. The parameter λ_x varies between 0.1 and 0.2: therefore, assuming the simulation-based rule $n_x \geq 2/\lambda_x$, the adopted mesh is characterized by $n_x = n_y = 20$. Interestingly, the relationship between the ratio $w_{\max}/w^0_{\max}$ and the parameter λ_x is perfectly linear for $\lambda_x \in [0.1, 0.2]$.

The stiffening effect is also enhanced as the aspect ratio L_y/L_x decreases, while maintaining a constant length-scale parameter $\lambda_x = L_c/L_x$ along the x-axis. In such cases, a reduction in L_y/L_x leads to an increase in the length-scale parameter $\lambda_y = L_c/L_y$ along the y-axis, thus diminishing the attenuation effect of the kernel function. This trend is illustrated in Fig. 16, where the ratio $w_{\max}/w^0_{\max}$ is plotted against L_y/L_x for CCCC rectangular nanoplates characterized by $\lambda_x = 0.05$ and

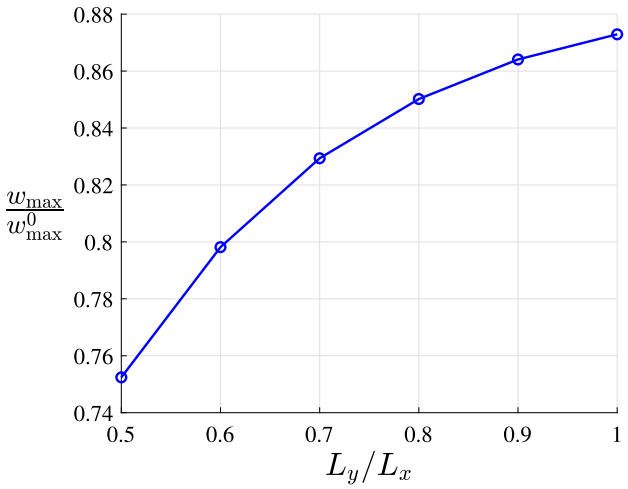

Fig. 16. The ratio $w_{\max}/w^0_{\max}$ plotted against L_y/L_x for CCCC rectangular nanoplates with $\lambda_x = 0.05$ and $\bar{q} = 1$.

subjected to $\bar{q} = 1$. The mesh is defined by $n_x = 30$ and $n_y = n_x L_y/L_x$, where only integer values of n_y are considered.

7. Concluding remarks

A general theoretical and computational framework has been developed for modeling and analysis of nanoplates. The Kirchhoff theory for local elastic plates has been first recalled. Then, the nonlocal elastic problem has been formulated for thin nanoplates on the basis of the stress-driven integral law of elasticity. It has been shown that the governing problem is represented by a set of integro-partial differential equations, which are generally difficult to solve. The solution methodologies available in the literature refer to a specific type of kernel and plate geometry. Here, a general solution procedure is proposed, based on the iterative algorithm conceived by Romano et al. [49]. The presented method consists of solving the nonlocal elastic problem by iteratively solving a sequence of local elastic problems. This simplified approach accommodates arbitrary geometries, kernel types, as well as general boundary and loading conditions, and can thus be adopted to model and design two-dimensional nanostructures based on nanoplates, such as smart devices and nanocoatings.

CRediT authorship contribution statement

Andrea Caporale: Writing – original draft, Supervision, Software, Methodology, Investigation, Formal analysis, Conceptualization, Validation. **Marzia Sara Vaccaro:** Writing – original draft, Software, Methodology, Investigation, Formal analysis, Conceptualization. **Raffaele Barretta:** Writing – original draft, Supervision, Software, Methodology, Investigation, Formal analysis, Conceptualization. **Raimondo Luciano:** Writing – original draft, Validation, Supervision, Methodology, Investigation, Formal analysis, Conceptualization.

Declaration of competing interest

The authors declare that they have no known competing financial interests or personal relationships that could have appeared to influence the work reported in this paper.

Acknowledgments

The research leading to these results has received funding from Project "P20223PLC2 - Nonlocal modelling of nano-coatings (NanoCo)" CUP H53D23008500001 funded by European Union in NextGenerationEU plan, Mission 4, Component 2, Investment 1.1 through the Italian "Bando Prin 2022 PNRR - D.D. 1409 of September 14, 2022" by MUR.

Appendix A. Kernels adopted in Section 6

The kernels adopted in this work, and reported in this appendix, are characterized by the following properties:

(i) they are non-negative;
(ii) their integral over the domain of integration (line or surface) equals one (normalization);
(iii) they are a delta sequence, i.e., they converge to the Dirac delta function as the internal characteristic length tends to zero.

The one-dimensional kernel adopted in Section 6.1 is

$$\psi(x,\tau)=\frac{1}{2l\tau}\exp\left(-\frac{|x|}{l\tau}\right), \tag{A.1}$$

where $\tau=e_0a/l$, e_0 is a material property, a represents an internal characteristic length, and l is an external characteristic length. Many works on nonlocal structures (see, e.g., [29,34,37,39,51]) have exploited the kernel (A.1) proposed by Eringen [22], substituting $l\tau$ with L_c and considering L_c as the length-scale parameter defining the nanostructure of the solid (in Section 6.1, it is assumed $L_c=l\tau$). For the one-dimensional kernel, the three properties introduced at the start of this appendix become:

(i) Non-negativity: $\psi(x,\tau)\geq 0$,
(ii) Normalization: $\int_{-\infty}^{\infty}\psi(x,\tau)dx=1$,
(iii) Impulsivity: $\lim_{\tau\to 0^+}\int_{-\infty}^{\infty}f(x')\,\psi(x-x',\tau)dx'=f(x)$.

A natural extension of the one-dimensional kernel (A.1) to two-dimensional nanostructures is

$$\psi(x,y,\tau)=\frac{1}{(2l\tau)^2}\exp\left(-\frac{|x|+|y|}{l\tau}\right), \tag{A.2}$$

which has been proposed by Farajpour et al. [48] for the nonlocal analysis of rectangular nanoplates. For a generic two-dimensional kernel, the three properties stated at the beginning of this appendix become:

(i) Non-negativity: $\psi(x,y,\tau)\geq 0$,
(ii) Normalization: $\int_{-\infty}^{\infty}\int_{-\infty}^{\infty}\psi(x,y,\tau)\,dxdy=1$,
(iii) Impulsivity: $\lim_{\tau\to 0^+}\int_{-\infty}^{\infty}\int_{-\infty}^{\infty}f(x',y')\,\psi(x-x',y-y',\tau)\,dx'dy'=f(x,y)$.

The fraction $1/(2l\tau)$ in (A.1) is due to normalization over the one-dimensional line, whereas the fraction $1/(2l\tau)^2$ in (A.2) comes from normalization over the two-dimensional plane. Therefore, the two kernels (A.1) and (A.2) can be considered to be of the same nature. The adoption of the kernel (A.2) is justified by its derivation from a one-dimensional kernel widely used in the literature on nonlocal nanobeams. However, it has a drawback: the argument $(-|x|-|y|)/(l\tau)$ of the exponential function is not invariant under coordinate transformations and therefore depends on the choice of coordinate system, even when referring to the same point (x,y).

An alternative two-dimensional kernel was proposed by Eringen [22] and is given by

$$\psi(x,y,\tau)=\frac{1}{\pi l^2\tau}\exp\left(-\frac{x^2+y^2}{l^2\tau}\right). \tag{A.3}$$

An advantage of (A.3) is that the argument $(-x^2-y^2)/(l^2\tau)$ of the exponential function contains the Euclidean distance of the point (x,y), which is invariant under coordinate transformation. The numerical applications presented in Section 6.2 are based on the assumption that $L_c=l\sqrt{\tau}$ for the kernel in Eq. (A.3).

Appendix B. Shape functions of the Melosh–Zienkiewicz–Cheung finite element

For the Melosh–Zienkiewicz–Cheung finite element, the transverse displacement in the square domain defined by $-1\leqslant\xi,\eta\leqslant 1$ is

$$\tilde{w}^e(\xi,\eta)=\hat{\boldsymbol{N}}(\xi,\eta)\,\tilde{\boldsymbol{u}}^e, \tag{B.1}$$

where

$$\hat{\boldsymbol{N}}=\left[\hat{N}_1,\ \hat{N}_2,\ \ldots\ \hat{N}_{12}\right], \tag{B.2}$$

with

$$\hat{N}_j(\xi,\eta)=\frac{1}{8}(1+\xi_i\xi)(1+\eta_i\eta)(2+\xi_i\xi+\eta_i\eta-\xi^2-\eta^2) \qquad \text{for } j=3(i-1)+1,$$
$$\hat{N}_j(\xi,\eta)=\frac{1}{8}(\xi^2-1)(\xi+\xi_i)(1+\eta_i\eta) \qquad \text{for } j=3(i-1)+2,$$
$$\hat{N}_j(\xi,\eta)=\frac{1}{8}(\eta^2-1)(\eta+\eta_i)(1+\xi_i\xi) \qquad \text{for } j=3(i-1)+3,$$

(ξ_i,η_i) the coordinates of the ith finite element vertex

$$(\xi_1,\eta_1)=(-1,-1),\ (\xi_2,\eta_2)=(1,-1),\ (\xi_3,\eta_3)=(1,1),\ (\xi_4,\eta_4)=(-1,1), \tag{B.3}$$

and

$$\tilde{\boldsymbol{u}}^e=\left[\tilde{\boldsymbol{u}}_1^e,\ \tilde{\boldsymbol{u}}_2^e,\ \tilde{\boldsymbol{u}}_3^e,\ \tilde{\boldsymbol{u}}_4^e\right]^{\mathrm{T}}, \tag{B.4}$$

with

$$\tilde{\boldsymbol{u}}_i^e=\left[(\tilde{w}^e)_i,\ \left(\frac{\partial\tilde{w}^e}{\partial x}\right)_i,\ \left(\frac{\partial\tilde{w}^e}{\partial y}\right)_i\right]. \tag{B.5}$$

The vector $\tilde{\boldsymbol{u}}_i^e$ contains the nodal parameters of displacement and rotation: $(\tilde{w}^e)_i$, $(\partial\tilde{w}^e/\partial x)_i$, and $(\partial\tilde{w}^e/\partial y)_i$ are, respectively, the transverse displacement w, the rotation θ_x around the y-axis, and the rotation θ_y around the x-axis evaluated at node i in finite element e.

Appendix C. Shape functions of the Bogner–Fox–Schmit finite element

The shape functions of the Bogner–Fox–Schmit (BFS) finite element are combinations of the Hermite interpolations. Specifically, the transverse displacement in the square domain defined by $-1\leqslant\xi,\eta\leqslant 1$ is

$$\tilde{w}^e(\xi,\eta)=\sum_{i=1}^{4}\hat{\boldsymbol{N}}_i(\xi,\eta)\,\tilde{\boldsymbol{u}}_i^e, \tag{C.1}$$

where

$$\begin{aligned}
\hat{\boldsymbol{N}}_1(\xi,\eta)&=\left[H_1^w(\xi)H_1^w(\eta),\ H_1^\theta(\xi)H_1^w(\eta),\ H_1^w(\xi)H_1^\theta(\eta),\ H_1^\theta(\xi)H_1^\theta(\eta)\right],\\
\hat{\boldsymbol{N}}_2(\xi,\eta)&=\left[H_2^w(\xi)H_1^w(\eta),\ H_2^\theta(\xi)H_1^w(\eta),\ H_2^w(\xi)H_1^\theta(\eta),\ H_2^\theta(\xi)H_1^\theta(\eta)\right],\\
\hat{\boldsymbol{N}}_3(\xi,\eta)&=\left[H_2^w(\xi)H_2^w(\eta),\ H_2^\theta(\xi)H_2^w(\eta),\ H_2^w(\xi)H_2^\theta(\eta),\ H_2^\theta(\xi)H_2^\theta(\eta)\right],\\
\hat{\boldsymbol{N}}_4(\xi,\eta)&=\left[H_1^w(\xi)H_2^w(\eta),\ H_1^\theta(\xi)H_2^w(\eta),\ H_1^w(\xi)H_2^\theta(\eta),\ H_1^\theta(\xi)H_2^\theta(\eta)\right],
\end{aligned} \tag{C.2}$$

with

$$\begin{aligned}
H_1^w(\xi)&=\frac{1}{4}\left(2-3\xi+\xi^3\right), & H_1^\theta(\xi)&=\frac{1}{4}\left(1-\xi-\xi^2+\xi^3\right),\\
H_2^w(\xi)&=\frac{1}{4}\left(2+3\xi-\xi^3\right), & H_2^\theta(\xi)&=\frac{1}{4}\left(-1-\xi+\xi^2+\xi^3\right),
\end{aligned} \tag{C.3}$$

and

$$\tilde{\boldsymbol{u}}_i^e=\left[(\tilde{w}^e)_i,\ \left(\frac{\partial\tilde{w}^e}{\partial x}\right)_i,\ \left(\frac{\partial\tilde{w}^e}{\partial y}\right)_i,\ \left(\frac{\partial^2\tilde{w}^e}{\partial x\partial y}\right)_i\right]^{\mathrm{T}}. \tag{C.4}$$

The first three components of $\tilde{\boldsymbol{u}}_i^e$ are described at the end of Appendix B. The last component $\left(\partial^2\tilde{w}^e/\partial x\partial y\right)_i$ is the derivative $\partial^2 w/\partial x\partial y$ evaluated at node i in finite element e. This is one of the most accurate rectangular finite elements for thin plates.

Appendix D. Bilinear shape functions for the element transformation

The shape functions in Eq. (41) are

$$\hat{N}_i(\xi,\eta) = \frac{1}{4}\left(1+\xi_i\xi\right)\left(1+\eta_i\eta\right) \quad \text{for } i = 1,2,3,4,$$

where the coordinates ξ_i and η_i are given in (B.3). In case of a mesh composed of rectangular finite elements, the calculations are significantly simplified: for instance, the Jacobian of the transformation in Eq. (41) is constant and given by

$$J = \frac{1}{4}\left(\tilde{x}_2^e - \tilde{x}_1^e\right)\left(\tilde{y}_4^e - \tilde{y}_1^e\right). \tag{D.1}$$

Appendix E. Boundary conditions on nodal parameters

The boundary conditions described in Section 6 require the nodal parameters to satisfy specific constraints, which depend on the type of finite element used. Further details are provided in the following list:

- Clamped nanoplates (CCCC).
  For the nanoplate discretized using MZC finite elements, the BCs given in Eq. (47) involve the following conditions on the nodal displacements and rotations of the finite element mesh:

$$\begin{cases} \tilde{w}(x_i^e, y_i^e) = \left.\dfrac{\partial\tilde{w}(x,y)}{\partial x}\right|_{\substack{x=x_i^e\\y=y_i^e}} = \left.\dfrac{\partial\tilde{w}(x,y)}{\partial y}\right|_{\substack{x=x_i^e\\y=y_i^e}} = 0 \\ \forall e \text{ and } \forall i \text{ such that } y_i^e = 0, L_y \text{ or } x_i^e = 0, L_x. \end{cases} \tag{E.1}$$

  For the nanoplate discretized using BFS finite elements, the BCs in Eq. (47) take the form:

$$\begin{cases} \tilde{w}(x_i^e, y_i^e) = \left.\dfrac{\partial\tilde{w}(x,y)}{\partial x}\right|_{\substack{x=x_i^e\\y=y_i^e}} = \left.\dfrac{\partial\tilde{w}(x,y)}{\partial y}\right|_{\substack{x=x_i^e\\y=y_i^e}} = \left.\dfrac{\partial^2\tilde{w}(x,y)}{\partial x\partial y}\right|_{\substack{x=x_i^e\\y=y_i^e}} = 0 \\ \forall e \text{ and } \forall i \text{ such that } y_i^e = 0, L_y \text{ or } x_i^e = 0, L_x. \end{cases} \tag{E.2}$$

  In Eqs. (E.1) and (E.2), the functions $\tilde{w}$, $\partial\tilde{w}/\partial x$, and $\partial\tilde{w}/\partial y$, evaluated at point (x_i^e, y_i^e), correspond to the nodal quantities $(\tilde{w}^e)_i$, $(\partial\tilde{w}^e/\partial x)_i$, and $(\partial\tilde{w}^e/\partial y)_i$, respectively, as defined in Eq. (B.5) of Appendix B and Eq. (C.4) of Appendix C. In Eq. (E.2), the function $\partial^2\tilde{w}/\partial x\partial y$, evaluated at point (x_i^e, y_i^e), correspond to the nodal quantity $\left(\partial^2\tilde{w}^e/\partial x\partial y\right)_i$ as defined in Eq. (C.4) of Appendix C. The conditions in Eqs. (E.1) and (E.2) enforce that appropriate nodal parameters in the FEM model vanish along the edges of the nanoplate.
- Simply supported nanoplates (SSSS).
  For the nanoplate discretized using MZC or BFS finite elements, the BCs given in Eq. (48) involve the following conditions on the nodal displacements and rotations of the finite element mesh:

$$\begin{cases} \tilde{w}(x_i^e, y_i^e) = \left.\dfrac{\partial\tilde{w}(x,y)}{\partial x}\right|_{\substack{x=x_i^e\\y=y_i^e}} = 0 \quad \forall e \text{ and } \forall i \text{ such that } y_i^e = 0, L_y, \\ \tilde{w}(x_i^e, y_i^e) = \left.\dfrac{\partial\tilde{w}(x,y)}{\partial y}\right|_{\substack{x=x_i^e\\y=y_i^e}} = 0 \quad \forall e \text{ and } \forall i \text{ such that } x_i^e = 0, L_x. \end{cases} \tag{E.3}$$

  The conditions in Eq. (E.3) enforce that appropriate nodal displacements and rotations in the FEM model vanish along the edges of the nanoplate.
- Nanoplates clamped at the edges parallel to the y-axis and free at the other edges (FCFC).
  For the nanoplate discretized using MZC finite elements, the BCs in Eq. (49) involve the following conditions on the nodal displacements and rotations of the finite element mesh:

$$\begin{cases} \tilde{w}(x_i^e, y_i^e) = \left.\dfrac{\partial\tilde{w}(x,y)}{\partial x}\right|_{\substack{x=x_i^e\\y=y_i^e}} = \left.\dfrac{\partial\tilde{w}(x,y)}{\partial y}\right|_{\substack{x=x_i^e\\y=y_i^e}} = 0 \\ \forall e \text{ and } \forall i \text{ such that } x_i^e = 0, L_x. \end{cases} \tag{E.4}$$

  For the nanoplate discretized using BFS finite elements, the BCs in Eq. (49) take the form:

$$\begin{cases} \tilde{w}(x_i^e, y_i^e) = \left.\dfrac{\partial\tilde{w}(x,y)}{\partial x}\right|_{\substack{x=x_i^e\\y=y_i^e}} = \left.\dfrac{\partial\tilde{w}(x,y)}{\partial y}\right|_{\substack{x=x_i^e\\y=y_i^e}} = \left.\dfrac{\partial^2\tilde{w}(x,y)}{\partial x\partial y}\right|_{\substack{x=x_i^e\\y=y_i^e}} = 0 \\ \forall e \text{ and } \forall i \text{ such that } x_i^e = 0, L_x. \end{cases} \tag{E.5}$$

- Nanoplates simply supported at the edges parallel to the y-axis and free at the other edges (FSFS).
  For the nanoplate discretized using MZC or BFS finite elements, the BCs in Eq. (50) involve the following conditions on the nodal displacements and rotations of the finite element mesh:

$$\tilde{w}(x_i^e, y_i^e) = \left.\frac{\partial\tilde{w}(x,y)}{\partial y}\right|_{\substack{x=x_i^e\\y=y_i^e}} = 0 \quad \forall e \text{ and } \forall i \text{ such that } x_i^e = 0, L_x. \tag{E.6}$$

Data availability

Data will be made available on request.

References

[1] S. Zhou, L. Qi, R. Zhang, A. Li, F. Ren, Z. Zheng, J. Qiao, Y. Sun, S. Zhou, Analysis of the electromechanical responses of sandwich circular nano-plate based on flexoelectric nano-ultrasonic transducer, Appl. Math. Model. 137 (2025) 115697.

[2] P. Nateghi-Babagi, B. Navayi-Neya, M. Eskandari-Ghadi, Free vibration and buckling analysis of simply supported rectangular nano-plates: A closed-form solution based on nonlocal 3D elasticity theory, Int. J. Solids Struct. 312 (2025) 113261.

[3] X. Wang, J. Yu, B. Zhang, L. Elmaimouni, L. Li, Lamb waves in piezoelectric quasicrystal multi-layered nano-plates with imperfect interfaces, Compos. Struct. 370 (2025) 119430.

[4] P. Xie, C. Chi, Y. Yang, F. Hong, H. Hao, S. Yan, SnO2 nanoplates via structural modulation enabling selective and sensitive NO2 detection at ppb level, Sensors Actuators B: Chem. 442 (2025) 138125.

[5] F. dell'Isola, I. Giorgio, M. Pawlikowski, N.L. Rizzi, Large deformations of planar extensible beams and pantographic lattices: heuristic homogenization, experimental and numerical examples of equilibrium, Proc. R. Soc. A: Math. Phys. Eng. Sci. 472 (2185) (2016) 20150790, http://dx.doi.org/10.1098/rspa.2015.0790.

[6] S.M. Hozhabrossadati, N. Challamel, M. Rezaiee-Pajand, A.A. Sani, Application of green's function method to bending of stress gradient nanobeams, Int. J. Solids Struct. 143 (2018) 209–217.

[7] E. Barchiesi, F. dell'Isola, F. Hild, On the validation of homogenized modeling for bipantographic metamaterials via digital image correlation, Int. J. Solids Struct. 208 (2021) 49–62, http://dx.doi.org/10.1016/j.ijsolstr.2020.11.003.

[8] L. Placidi, L. Greco, S. Bucci, E. Turco, N. Rizzi, A second gradient formulation for a 2D fabric sheet with inextensible fibres, Z. Für Angew. Math. Und Phys. 67 (2016) http://dx.doi.org/10.1007/s00033-016-0701-8.

[9] L. Placidi, M.G.E. Sherbiny, P. Baragatti, Experimental investigation for the existence of frequency band gap in a microstructure model, Math. Mech. Complex Syst. 9 (4) (2022) 413–421.

[10] L. Placidi, F. dell'Isola, A. Kandalaft, R. Luciano, C. Majorana, A. Misra, A granular micromechanic-based model for ultra high performance fiber-reinforced concrete (uhp frc), Int. J. Solids Struct. 297 (2024) 112844, http://dx.doi.org/10.1016/j.ijsolstr.2024.112844.

[11] R. Izadi, R. Das, N. Fantuzzi, P. Trovalusci, Fracture properties of green nano fibrous network with random and aligned fiber distribution: A hierarchical molecular dynamics and peridynamics approach, Internat. J. Engrg. Sci. 204 (2024).
[12] D.G. Özdemir, N. Evcimen Duygulu, A.C. Özarslan, F. Ciftci, Fabrication and characterization of Graphene oxide/Fucoidan/Chitosan reinforced Poly(vinyl alcohol) nanocomposites, J. Mol. Struct. 1301 (2024) 137330.
[13] A. Rezaei, R. Izadi, N. Fantuzzi, A non-classical computational method for modelling functionally graded porous planar media using micropolar theory, Comput. Struct. 306 (2025).
[14] R. Penna, G. Lovisi, Surface and nonlocal effects in piezoelectric nanobeams, Eur. J. Mech. A Solids 113 (2025) 105715.
[15] H. Nguyen, N. Challamel, C. Wang, Analytical solutions for free vibrations of rectangular cuboid elastic lattices and their continuous approximations, J. Sound Vib. 600 (2025) 118836.
[16] E. Kröner, Elasticity theory of materials with long range cohesive forces, Int. J. Solids Struct. 3 (5) (1967) 731–742.
[17] J.A. Krumhansl, Some considerations of the relation between solid state physics and generalized continuum mechanics, in: E. Kröner (Ed.), Mechanics of Generalized Continua, Springer Berlin Heidelberg, Berlin, Heidelberg, 1968, pp. 298–311.
[18] I.A. Kunin, The theory of elastic media with microstructure and the theory of dislocations, in: E. Kröner (Ed.), Mechanics of Generalized Continua, Springer Berlin Heidelberg, Berlin, Heidelberg, 1968, pp. 321–329.
[19] D. Rogula, Influence of spatial acoustic dispersion on dynamical properties of dislocations, Bull. Pol. Acad. Sci.: Tech. Sci. 13 (1965) 337–385.
[20] D. Rogula, Introduction to nonlocal theory of material media, in: D. Rogula (Ed.), Nonlocal Theory of Material Media, Springer Vienna, Vienna, 1982, pp. 123–222.
[21] A.C. Eringen, Linear theory of nonlocal elasticity and dispersion of plane waves, Internat. J. Engrg. Sci. 10 (1972) 425–435.
[22] A.C. Eringen, On differential equations of nonlocal elasticity and solutions of screw dislocation and surface waves, J. Appl. Phys. 54 (9) (1983) 4703–4710.
[23] J. Peddieson, G.R. Buchanan, R.P. McNitt, Application of nonlocal continuum models to nanotechnology, Internat. J. Engrg. Sci. 41 (3–5) (2003) 305–312.
[24] N. Challamel, C.M. Wang, The small length scale effect for a non-local cantilever beam: a paradox solved, Nanotechnology 19 (34) (2008) 345703.
[25] E. Benvenuti, A. Simone, One-dimensional nonlocal and gradient elasticity: Closed-form solution and size effect, Mech. Res. Commun. 48 (2013) 46–51.
[26] P. Khodabakhshi, J. Reddy, A unified integro-differential nonlocal model, Internat. J. Engrg. Sci. 95 (2015) 60–75, URL: https://www.sciencedirect.com/science/article/pii/S0020722515000919.
[27] G. Romano, R. Barretta, M. Diaco, F.M. de Sciarra, Constitutive boundary conditions and paradoxes in nonlocal elastic nanobeams, Int. J. Mech. Sci. 121 (2017) 151–156.
[28] G. Romano, R. Barretta, Nonlocal elasticity in nanobeams: the stress-driven integral model, Internat. J. Engrg. Sci. 115 (2017) 14–27.
[29] M. Rezaiee-Pajand, N. Rajabzadeh-Safaei, Stress-driven nonlinear behavior of curved nanobeams, Internat. J. Engrg. Sci. 178 (2022) 103724.
[30] P. Zhang, P. Schiavone, H. Qing, Stress-driven local/nonlocal mixture model for buckling and free vibration of FG sandwich Timoshenko beams resting on a nonlocal elastic foundation, Compos. Struct. 289 (2022) 115473.
[31] M.S. Vaccaro, F.P. Pinnola, F. Marotti de Sciarra, M. Ĉanađija, R. Barretta, Stress-driven two-phase integral elasticity for Timoshenko curved beams, Proc. Inst. Mech. Eng. Part N: J. Nanomater. Nanoeng. Nanosyst. 235 (1–2) (2021) 52–63.
[32] R. Barretta, M. Ĉanađija, R. Luciano, F. Marotti de Sciarra, On the mechanics of nanobeams on nano-foundations, Internat. J. Engrg. Sci. 180 (2022) 103747.
[33] A. Caporale, R. Luciano, D. Scorza, S. Vantadori, Local–nonlocal stress-driven model for multi-cracked nanobeams, Int. J. Solids Struct. 273 (2023) 112230.
[34] M. Jafarinezhad, R. Sburlati, R. Cianci, Static and free vibration analysis of functionally graded annular plates using stress-driven nonlocal theory, Eur. J. Mech. A Solids 99 (2023) 104955.
[35] G. Lovisi, Application of the surface stress-driven nonlocal theory of elasticity for the study of the bending response of FG cracked nanobeams, Compos. Struct. 324 (2023) 117549.
[36] S. Wang, W. Ding, Z. Li, B. Xu, C. Zhai, W. Kang, W. Yang, Y. Li, A size-dependent quasi-3D model for bending and buckling of porous functionally graded curved nanobeam, Internat. J. Engrg. Sci. 193 (2023) 103962.
[37] G. Lovisi, L. Feo, A. Lambiase, R. Penna, Application of surface stress-driven model for higher vibration modes of functionally graded nanobeams, Nanomaterials 14 (4) (2024) 350.
[38] D. Indronil, Dynamics of nonlocal stress-driven Rayleigh beam, Forces Mech. 18 (2025) 100299.
[39] G. Alotta, A.F. Russillo, G. Failla, Elastic wave propagation in periodic stress-driven nonlocal timoshenko beams, Int. J. Solids Struct. 306 (2025) 113103.
[40] M.-S. Behnam-Rasouli, N. Challamel, A. Karamodin, A.A. Sani, Application of the green's function method for static analysis of nonlocal stress-driven and strain gradient elastic nanobeams, Int. J. Solids Struct. 295 (2024) 112794.
[41] N. Challamel, A.A. Sani, Green's functions of size-dependent timoshenko beams: Gradient elasticity versus stress-driven nonlocal theories, Int. J. Solids Struct. 314 (2025) 113308.
[42] R. Barretta, F. Marotti de Sciarra, M.S. Vaccaro, Nonlocal elasticity for nanostructures: A review of recent achievements, Encyclopedia 3 (2023) 279–310, http://dx.doi.org/10.3390/encyclopedia3010018.
[43] R. Barretta, S.A. Faghidian, F. Marotti de Sciarra, Stress-driven nonlocal integral elasticity for axisymmetric nano-plates, Internat. J. Engrg. Sci. 136 (2019) 38–52.
[44] M.S. Vaccaro, H.M. Sedighi, Two-phase elastic axisymmetric nanoplates, Eng. Comput. 39 (2023) 827–834.
[45] M. Jafarinezhad, R. Sburlati, R. Cianci, Static and free vibration analysis of functionally graded annular plates using stress-driven nonlocal theory, Eur. J. Mech. A Solids 99 (2023).
[46] R. Cianci, M. Jafarinezhad, R. Sburlati, A Gauss kernel non-local stress-driven plate theory, Compos. Struct. 351 (2025).
[47] M. Jafarinezhad, R. Sburlati, R. Cianci, Nonlocal stress-driven model for functionally graded mindlin annular plate: bending and vibration analysis, Arch. Appl. Mech. 94 (5) (2024) 1313–1333.
[48] A. Farajpour, C.Q. Howard, W.S.P. Robertson, On size-dependent mechanics of nanoplates, Internat. J. Engrg. Sci. 156 (2020) 103368.
[49] G. Romano, R. Barretta, M. Diaco, Iterative methods for nonlocal elasticity problems, Contin. Mech. Thermodyn. 31 (2019) 669–689.
[50] S. Timoshenko, S. Woinowsky-Krieger, Theory of Plates and Shells, McGraw-Hill, New York, 1959.
[51] G. Romano, R. Barretta, M. Diaco, On nonlocal integral models for elastic nano-beams, Int. J. Mech. Sci. 131–132 (2017) 490–499.